

# Self-Assembly of Mn<sub>3</sub>O<sub>4</sub> Nanoparticles into Mesoporous Microstructures for Use as Supercapacitor Electrode Material

Venugopal Nulu, Ji Seong Moon, Won Wook Park, HanJung Song, and Keun Yong Sohn\*

Department of Nanoscience and Engineering, Center for Nano Manufacturing, Inje University, 197 Inje-ro, Gimhae, Gyeongnam-do 50834, Republic of Korea

\*E-mail: [ksohn@inje.ac.kr](mailto:ksohn@inje.ac.kr); [ksohnlab@gmail.com](mailto:ksohnlab@gmail.com)

*Received:* 4 June 2018 / *Accepted:* 11 July 2018 / *Published:* 5 August 2018

---

The exceptional and unusual properties of hierarchically structured inorganic materials have led to a major push forward in related research and development. In the present study, a simple modified version of the room-temperature one-pot co-precipitation method was employed to synthesize Mn<sub>3</sub>O<sub>4</sub> nanoparticles which then self-aggregated into mesoporous microstructures. The obtained structures were used as for the electrodes in electrochemical capacitors. The as-obtained Mn<sub>3</sub>O<sub>4</sub> microstructures exhibited acceptable specific capacitances of 260 and 180 F g<sup>-1</sup> at current densities of 1 and 5 A g<sup>-1</sup>, respectively, with 98% capacity retention after 2000 cycles.

---

**Keywords:** chemical method; microstructures; supercapacitors; specific capacitance

## 1. INTRODUCTION

In recent years, manganese oxides, which are extremely interesting materials that exist in several structural forms and in various Mn oxidation states, have attracted great scientific interest because of their physical and chemical properties [1, 2]. Among these Mn-based oxides, Mn<sub>3</sub>O<sub>4</sub> has been used as a catalyst in the reduction of NO<sub>x</sub> and oxidation by CO [3]. In particular, Mn<sub>3</sub>O<sub>4</sub> has been increasingly used as a supercapacitor electrode material because of the different oxidation states exhibited by Mn in Mn<sub>3</sub>O<sub>4</sub> (Mn<sup>2+</sup>(Mn<sup>3+</sup>)<sub>2</sub>O<sub>4</sub>), its high specific capacitance, eco-friendly nature, and low manufacturing cost [4, 5]. Recent research has demonstrated that materials with a wide variety of nanostructures can be applied as efficient electrode materials for supercapacitors, but there is still demand for new structures that can provide sufficient Faradaic reactions between the electrode and the electrolyte. Very recently, the synthesis of meso- and nano-structured metal oxides has produced appealing structures with a high surface area, a large number of reactive surface sites, and structural stability. Although great efforts have also been devoted to the development of materials with a high specific capacitance, there remains a need for new electrode materials that can deliver enhanced

electrochemical performance. It is worth noting that the synthesis of  $\text{Mn}_3\text{O}_4$  nanostructures via approaches such as hydrothermal and sol-gel methods has relatively low yield and incurs complex synthesis parameters. Furthermore, the resulting product requires further treatment to obtain a pure product. Therefore, to avoid the need for complex, sophisticated equipment, high-temperature reaction conditions, and the use of organic templates, while simultaneously reducing the cost of synthesis, there is a need to develop a simple, reliable means of synthesizing a pure  $\text{Mn}_3\text{O}_4$  phase at (most importantly) room temperature.

Herein, we report on a simple co-precipitation approach to the synthesis of  $\text{Mn}_3\text{O}_4$  porous microstructures at room temperature (RT), which does not require the use of any additional surfactant or a template. A > 90% dark brown powder was obtained at the gram-scale, which proved to be applicable as an efficient supercapacitor electrode material.

## 2. EXPERIMENT

### 2.1 Material Synthesis

All the chemicals acquired for the study were analytical grade and used without further purification. The preparation process is shown in scheme 1. First, 0.01 M  $(\text{CH}_3\text{COO})_2\text{Mn}\cdot 4\text{H}_2\text{O}$  was dissolved in ethanol and stirred with a magnetic stirrer for 20 min. Next, a 1 M KOH solution was separately prepared in deionized water, added to the solution of Mn(II) in ethanol over 30 min. The mixture was then stirred continuously for 6 h at room temperature, with the reaction beaker left uncovered and open to ambient air. After 6 h, the resulting brown precipitate was collected and washed several times with deionized water and absolute ethanol to remove any impurities. The final product was air dried at room temperature for 24 h. Based on similar soft chemical reactions that were previously reported for metal acetates and hydroxides in alcohols [5, 6], we hypothesized that the formation of  $\text{Mn}_3\text{O}_4$  proceeded as defined by the following equations. Oxygen obtained from the air and hydroxyl groups probably acted as the main oxidization sources of the metal ions during the reaction defined by Eq. (2). The final yield of the reaction was about 92%.



where  $x = (\text{OAc}^-)(\text{KOH})\cdot\text{H}_2\text{O}$  and was the surface ligand on the outer surface of the nanoparticles.

### 2.2 Characterization

The morphology and microstructures of the  $\text{Mn}_3\text{O}_4$  samples were examined by scanning electron microscopy (SEM; JSM7000F, JEOL, Japan), high-resolution transmission electron

microscopy (HR-TEM; JEM-2100F, JEOL, Japan), and energy-dispersive X-ray (EDX) spectroscopy. The crystalline structure of the materials was examined by powder X-ray diffraction (XRD), using a diffractometer (D/MAX-2200 Ultima, Rigaku, Japan) with Cu K $\alpha$  radiation ( $\lambda = 1.54056 \text{ \AA}$ ) over a range of  $10^\circ < 2\theta < 80^\circ$ , while operating at 30 kV and 40 mA. The N $_2$  adsorption–desorption isotherms were measured using a physisorption analyzer (ASAP 2020, Micromeritics, USA) at 77 K, and the surface areas of the samples were calculated using the Brunauer–Emmett–Teller (BET) method.

All of the electrochemical properties were measured in a three-electrode configuration, with 1 M Na $_2$ SO $_4$  as the electrolyte. The working electrode consisted of a stainless-steel foil as the current collector and a mixture of Mn $_3$ O $_4$  powder (70 wt%), acetylene black (20 wt%), and polyvinylidene difluoride (PVDF) (10 wt%). The reference electrode and counter electrode were a saturated calomel electrode (SCE) and a platinum sheet, respectively. Cyclic voltammetry (CV) was conducted using an electrochemical workstation (PARSTAT2273, Princeton Applied Research, USA) within a potential range of 0 to 1.2 V. Galvanostatic charge–discharge (GCD) experiments were performed at room temperature over a potential range of 0–0.5 V, using a potentiostat/galvanostat workstation (IviumStat, Ivium Technologies, The Netherlands). The following equation was used to calculate the specific capacitance ( $C_s$ ):

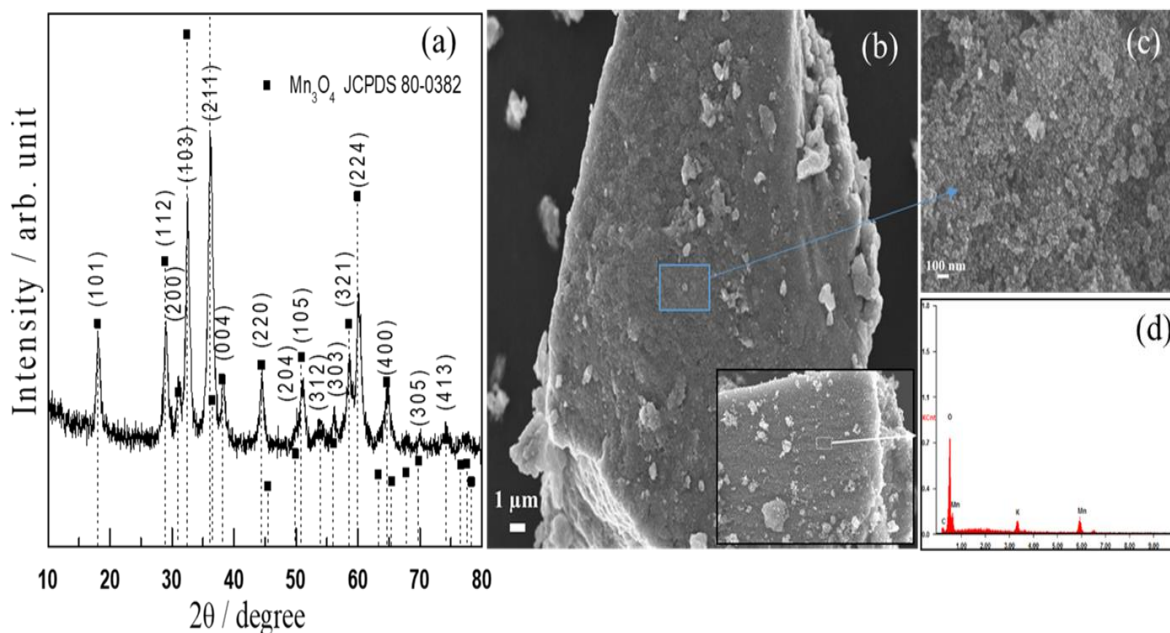
$$C_s = (I\Delta t) / (m\Delta V) , \quad (3)$$

where  $I$  (mA) is the current used for charge–discharge,  $\Delta t$  (s) is the time that elapses for the discharge cycle,  $m$  is the weight of the active electrode, and  $\Delta V$  is the potential drop during discharge.

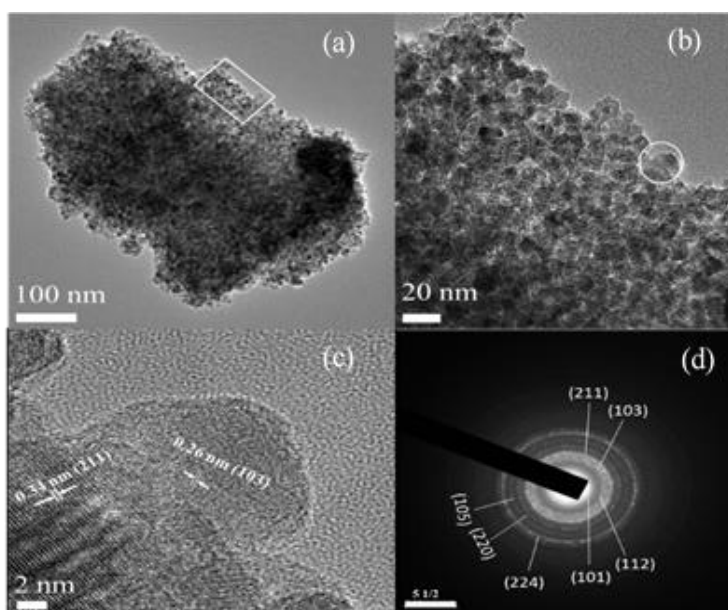
### 3. RESULTS AND DISCUSSION

Fig. 1a shows the XRD pattern of the as-obtained powder, in which all the diffraction features are well matched with those of hausmannite Mn $_3$ O $_4$  (JCPDS card no: 80-0382), indicating that a pure tetragonal phase of Mn $_3$ O $_4$  was successfully synthesized. Fig. 1b shows a low-magnification SEM image of a single micrometer-sized particle of our sample, with an apparent length, width, and height of 25, 15, and 10  $\mu\text{m}$ , respectively. The outside surface was accompanied by small secondary particles, all of which were irregular in shape and size, whereas a high-magnification SEM image of the marked region on a specific microbundle (shown in Fig. 1c) displays randomly arranged porous aggregates of nanoparticles. The inset in Fig. 1b is a field-emission SEM (FESEM) image of another selected microparticle, and the EDX elemental mapping (Fig. 1d) of the marked region (white box in the inset of Fig. 1b) of this microparticle exhibits clean Mn and O peaks. In addition, the morphology of the Mn $_3$ O $_4$  sample that was synthesized at room temperature was observed by obtaining TEM and HRTEM images, shown in Fig. 2. The TEM image of a specific microparticle (Fig. 2a) indicates that it was composed of self-assembled aggregates of well-formed crystalline nanoparticles with voids between them. A high-magnification view of a selected region (within the box in Fig. 2a) of these self-assembled nanoparticles, as shown in Fig. 2b, show that they had a narrow size distribution, with an average size of about 10 nm, and relatively good crystallinity. An HR-TEM image (Fig. 2c) reveals the crystalline nature of two adjacent nanoparticles marked by a white circle in Fig. 2b, indicating that the atomic lattice fringe spacings of 0.26 and 0.34 nm are in good agreement with the (103) and (211)

planes, respectively, of tetragonal  $Mn_3O_4$  (JCPDS card no: 80-0382). The selected-area electron-diffraction pattern (SAED) of our sample is also a good match with that of the tetragonal  $Mn_3O_4$  phase with strong ring patterns due to the (101), (103), (211), (220), (224), and (400) planes. This result is consistent with the XRD pattern discussed above (Fig. 1a).



**Figure 1.** (a) XRD pattern and (b) SEM image of a selected microparticle (the inset is a magnified FESEM image of another specific particle). (c) High-magnification SEM image captured at the selected portion of a microparticle (marked with the colored box in Fig. 1b); the inset shows a cross-sectional SEM image of the microparticle. (d) EDX elemental mapping of the selected area marked by the white box shown in the inset in Fig. 1b.



**Figure 2:** TEM images of a) a specific microparticle b) high-magnification TEM image of the selected portion in image (a), as indicated by the box, c) HRTEM image of selected nanoparticle,

indicated by the circle in image (b), d) Corresponding SAED pattern acquired at the position indicated by the rectangle in image (a).

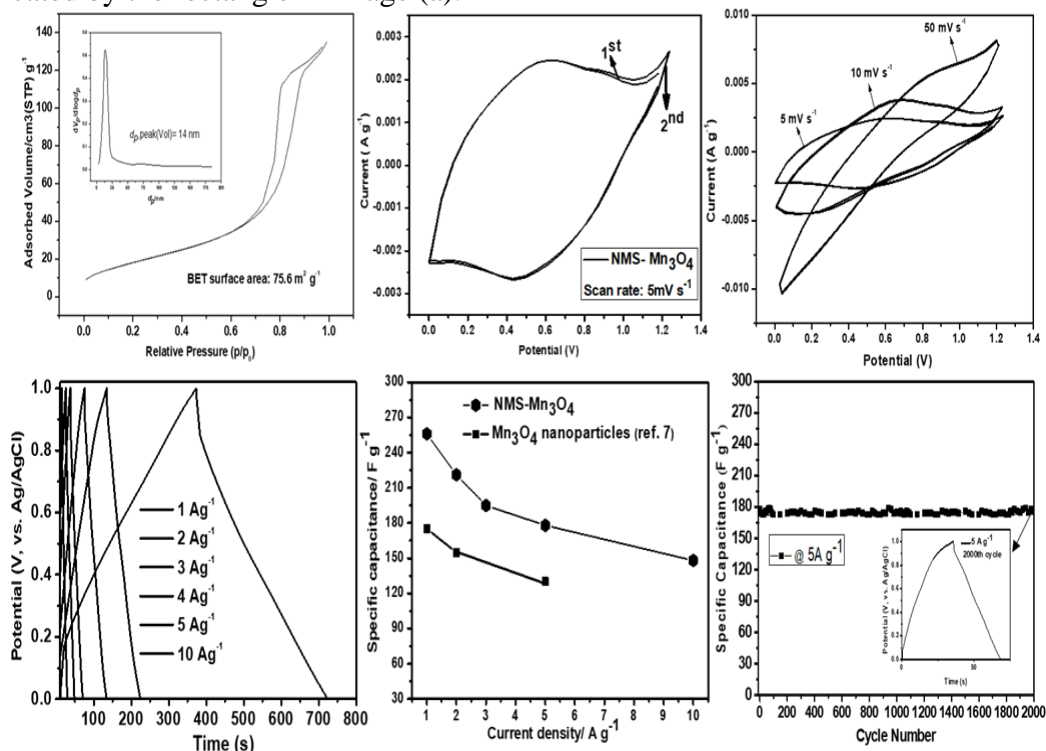


**Figure 3.** (a)  $N_2$  adsorption–desorption isotherms of as-obtained NMS- $Mn_3O_4$ ; inset shows the pore-size distribution. First two cyclic voltammograms curves at (b)  $5\text{ mV s}^{-1}$  and (c) different scanning rates. (d) Charge–discharge profiles at various current densities. (e) Specific capacitance as a function of current density. (f) Cycling performance over 2000 cycles at a current density of  $5\text{ A g}^{-1}$ ; inset shows the charge–discharge profile of the 2000<sup>th</sup> cycle.

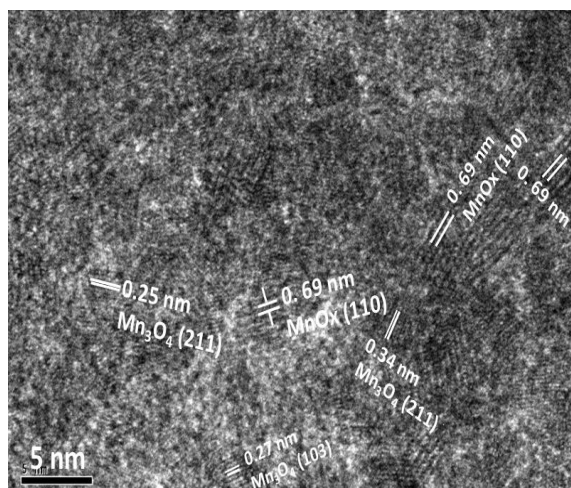
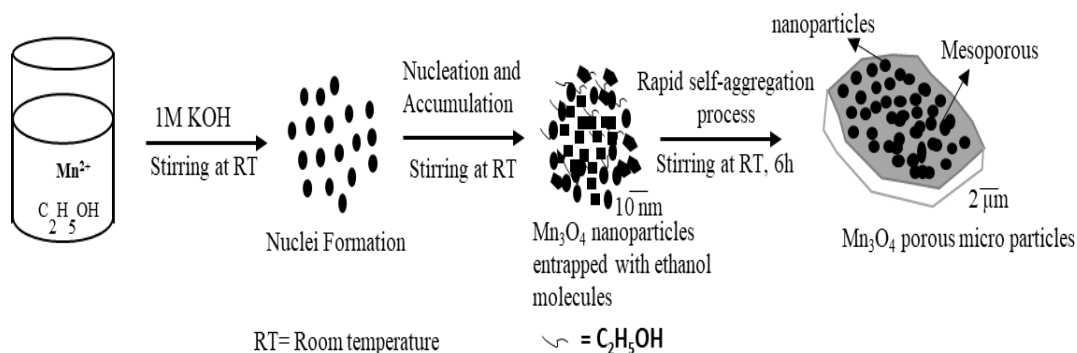


**Figure 4.** HRTEM image of analyzed sample collected after ten consecutive charge–discharge cycles.

We can conclude that our room-temperature approach resulted in pure-phase  $Mn_3O_4$  with good crystallinity, and we believe that the structures obtained were completely different from those described in previous reports [2-6].

Figure 3a shows the representative N<sub>2</sub> adsorption–desorption isotherm and Barrett–Joyner–Halenda (BJH) pore-size distribution plot (inset) of our Mn<sub>3</sub>O<sub>4</sub> material. The BJH method with the desorption branch clearly reveals the presence of mesopores with sizes in a range of 10–20 nm (average: ca. 14 nm). The measured BET surface area was ca. 75.6 m<sup>2</sup> g<sup>-1</sup>. The special textural properties would greatly enhance its physical and chemical properties, particularly in terms of its electrochemical performance in energy-storage applications. Hereafter, the nanoparticles that self-aggregated into microstructures of Mn<sub>3</sub>O<sub>4</sub> are referred to as NMS-Mn<sub>3</sub>O<sub>4</sub>.



**Scheme 1.** Schematic representation of the synthesis of Mn<sub>3</sub>O<sub>4</sub> porous microstructures.

Scheme 1 represents the synthesis process. First, the continuous stirring of manganese acetate in an ethanol solution in the absence of any alkaline raw material at room temperature produced Mn<sup>2+</sup>–organic species. The color of the resulting precipitate was a light pink, which became dark brown after the drop-wise addition of 1 M KOH; the initial pH of the solution was 10, which increased to 12 after the completion of the reaction. It is believed that the prolonged hydrolysis of the Mn<sup>2+</sup> species produced Mn<sub>3</sub>O<sub>4</sub>, as defined by Eqs. (1) and (2). As described earlier, a part of the precipitate was oxidized in air, causing the color to become dark brown. During the addition of 1 M KOH to the reaction mixture, nucleation took place initially and tiny nanoparticles or nanoclusters were formed owing to the accumulation of the nuclei. During this process, the ethanol molecules from the solvent were adsorbed onto the surfaces of the nanoparticles, such that they acted as soft capping agents. Under strong basic conditions owing to the minimization of interfacial energies, these tiny particles instinctively aggregated into larger, continuous, porous agglomerates. We believe that the adsorbed organic alcohol molecules had a tendency to generate spaces between the aggregated nanoparticles. Further stirring of this precipitate at RT led to the self-aggregation of the Mn<sub>3</sub>O<sub>4</sub> nanoparticles, leaving some void spaces between them and resulting in mesoporous microparticles, as shown in Scheme 1. We noticed a similar class in earlier reports on alcohol-mediated synthetic methods used to obtain metal oxide nanostructures, for which the size and shape control was accredited to the adsorbed solvent molecules and to the salt-solvent diffusion boundary coating the surfaces of the resultant nanostructures [7].

The electrochemical properties of the Mn<sub>3</sub>O<sub>4</sub> nanoparticles were obtained by conducting cyclic voltammetry (CV) and galvanostatic charge–discharge (GCD) tests, using an aqueous 1 M Na<sub>2</sub>SO<sub>4</sub>

solution as the electrolyte. The CV curves of the first 10 cycles at  $10 \text{ mV s}^{-1}$  appear to be stable. Figure 3b shows two consecutive CV curves of the NMS-Mn<sub>3</sub>O<sub>4</sub> electrode measured at  $5 \text{ mV s}^{-1}$  within the voltage limit of 0–1.2 V; both CV curves are broad and exhibit minor redox peaks (a cathodic peak at 0.42 V and an anodic peak at 0.58 V), and the broad area between the anodic and cathodic peaks clearly indicates excellent capacitive behavior. Fig. 3c shows two successive CV curves for the electrode measured at scanning rates of 5, 10, and  $50 \text{ mV s}^{-1}$ ; all the curves are broader and exhibit mirror-image features, indicating excellent capacitive behavior. The GCD curves of the NMS-Mn<sub>3</sub>O<sub>4</sub> electrode measured at current densities of 1, 2, 3, 5, and  $10 \text{ A g}^{-1}$  are shown in Fig. 3d, and excellent specific capacitances of 260, 225, 194, 180, and  $148 \text{ F g}^{-1}$  were observed at the respective applied current densities. When the current density was increased from 1 to  $5 \text{ A g}^{-1}$ , about 68% capacity retention was observed, compared to a 55% capacity retention at  $10 \text{ A g}^{-1}$ . This result is an indication of the good rate capability of the electrode (see Fig. 3e). Fig. 3f clearly shows that the NMS-Mn<sub>3</sub>O<sub>4</sub> electrode showed good cycling stability at  $5 \text{ mV s}^{-1}$  for over 2000 GCD cycles ( $176 \text{ F g}^{-1}$ ), with more than 96% retention of the capacity when compared to the capacitance of the first cycle ( $178 \text{ F g}^{-1}$ ). The inset in Fig. 3f shows the GCD profile for the 2000<sup>th</sup> cycle, which is quite similar to the GCD curve at the same current density shown in Fig. 3d, pointing to the good electrochemical stability of the electrode. In summary, the NMS-Mn<sub>3</sub>O<sub>4</sub> electrode exhibited excellent rate capability and good cycling stability relative to previously reported Mn<sub>3</sub>O<sub>4</sub>-based electrodes [8-16]. Table 1 compares the specific capacitance of our NMS-Mn<sub>3</sub>O<sub>4</sub> electrode material with those of recently reported Mn<sub>3</sub>O<sub>4</sub> nanostructures and their composites. To elucidate the structural morphology and the phase change of the porous Mn<sub>3</sub>O<sub>4</sub> nanoflakes after cycling, we undertook a TEM analysis of the electrode that was collected and washed with *N*-methyl pyrrolidone (NMP) to remove the binder PVDF after ten consecutive cycles (see Fig. 4). The TEM results, shown in Fig. 4, reveal the atomic lattice fringe spacing of the resultant nanoparticles to be 0.69, 0.25, and 0.34 nm, which is in good agreement with the MnO<sub>x</sub> (110) [17], Mn<sub>3</sub>O<sub>4</sub> (103), and Mn<sub>3</sub>O<sub>4</sub> (211) planes, respectively, indicating that post-cycling oxidation of the Mn<sup>3+</sup> to Mn<sup>4+</sup> occurs at the working electrode, which significantly affects the formation of the MnO<sub>x</sub> ( $x \sim 2$ ) phase together with Mn<sub>3</sub>O<sub>4</sub>. However, the electrochemical mechanism of our cycled electrode needs further investigation. Meanwhile, the shape of the aggregated porous nanoparticles is preserved.

**Table 1.** Comparison of specific capacitance of NMS-Mn<sub>3</sub>O<sub>4</sub> with those of other Mn<sub>3</sub>O<sub>4</sub> nanostructures.

Material	Electrolyte	Specific capacitance ( $\text{F g}^{-1}$ )	Reference
NMS-Mn <sub>3</sub> O <sub>4</sub>	1 M Na <sub>2</sub> SO <sub>4</sub>	260	This work
Mn <sub>3</sub> O <sub>4</sub> nanoparticles	1 M Na <sub>2</sub> SO <sub>4</sub>	210	[7]
Mn <sub>3</sub> O <sub>4</sub> /graphene	1 M Na <sub>2</sub> SO <sub>4</sub>	230	[9]
Mn <sub>3</sub> O <sub>4</sub> nanocrystals	1 M Na <sub>2</sub> SO <sub>4</sub>	211	[11]

Mn <sub>3</sub> O <sub>4</sub> /graphene	1 M Na <sub>2</sub> SO <sub>4</sub>	175	[8]
Mn <sub>3</sub> O <sub>4</sub> nanoparticles	1 M Na <sub>2</sub> SO <sub>4</sub>	171	[13]
Mn <sub>3</sub> O <sub>4</sub> /graphene	1 M Na <sub>2</sub> SO <sub>4</sub>	171	[14]

The above results confirm that the synthesized microstructures consisting of self-assembled fine Mn<sub>3</sub>O<sub>4</sub> nanoparticles were mesoporous in nature. These structural features would provide ideal supercapacitor electrode characteristics, including a high surface area, porosity for good electrolyte mobility, and structural rigidity, all of which are helpful to delivering a high specific capacitance at high current densities and maintaining a stable cycle life.

#### 4. CONCLUSIONS

A simple, room-temperature approach was successfully used to synthesize Mn<sub>3</sub>O<sub>4</sub> nanoparticles with sizes of about 5–10 nm that self-assembled into mesoporous microparticles. Without the use of any surfactant or template, the product exhibited high purity and good crystallization. The resultant structures featured optimized electrochemical activity with a high specific capacitance, rate capability, and long life span, all of which make the material an excellent choice for the electrodes of supercapacitors. The enhanced electrochemical performance may be a result of the uneven three-dimensional microstructures that result from the self-aggregates of nanoparticles interconnecting, with mesoscale void spaces between them. In addition, these structural benefits and the high product yield mean that our convenient synthesis route may also be applicable to the synthesis of other metal oxides.

#### ACKNOWLEDGEMENTS

This work was supported by the 2016 Post-doctoral Research Program of Inje University. The research was also supported by the Basic Science Research Program through the National Research Foundation of Korea (NRF) funded by the Ministry of Education (NRF-2015R1D1A1A01059983).

#### AUTHOR CONTRIBUTIONS

Keun Yong Sohn, Won Wook Park, HanJung Song and Venugopal Nulu drafted the manuscript. Venugopal Nulu designed the experiments and prepared and characterized all the samples. Ji Seong Moon and others performed the electrochemical measurements and analyzed the results.

#### CONFLICTS OF INTEREST

The authors declare no conflict of interest.

#### References

1. M. J. Deng, P. J. Ho, C. Z. Song, S. A. Chen, J. F. Lee, J. M. Chen, K. T. Lu, *Energy Environ. Sci.*, 6 (2013) 2178.
2. C. Wu, R. Brescia, M. Prato, S. Marras, L. Manna, M. Colombo, *J. Mater. Chem.*, 4 (2016) 18075.
3. Y. Luo, T. Yang, Z. Li, B. Xiao, M. Zhang, *Mater. Lett.*, 178 (2016) 171.
4. L. Wang, L. Chen, Y. Li, H. Ji, G. Yang, *Powder Techn.*, 235 (2013) 76.

5. S. J. Folkman, M. Zhou, M. Nicki, R. G. Finke, *Inorg. Chem.*, 57 (2018) 1517.
6. Y. Dong, K. He, L. Yin, A. Zhang, *Nanotechnology.*, 18 (2007) 435602.
7. T. He, D. Chen, X. Jiao, Y. Wang, Y. Duan, *Chem. Mater.*, 17 (2005) 4023.
8. X. Zhang, P. Yu, D. Zhang, H. Zhang, X. Sun, Y. Ma, *Mater. Lett.*, 92 (2013) 401.
9. B. Wang, J. Park, C. Wang, H. Ahn, G. Wang, *Electrochim. Acta.*, 55 (2010) 6812.
10. Y. Wu, S. Liu, H. Wang, X. Wang, X. Zhang, G. Jin, *Electrochim. Acta.*, 90 (2013) 210.
11. G. Xu, J. Shi, W. Dong, Y. Wen, X. Min, A. Tang, *J. Alloys Compd.*, 630 (2015) 266.
12. H.W. Park, H. J. Lee, S.-M. Park, K. C. Roh, *RSC Adv.*, 6 (2016) 18191.
13. X. Zhang, P. Yu, D. Zhang, H. Zhang, X. Sun, Y. Ma, *Mater. Lett.*, 92 (2013) 401.
14. S. Xing, Z. Zhou, Z. Ma, Y. Wu, *Mater. Lett.*, 65 (2011) 517.
15. Y. Fan, X. Zhang, Y. Liu, Q. Cai, J. Zhang, *Mater. Lett.*, 95 (2013) 153.
16. X. Zhang, X. Sun, Y. Chen, D. Zhang, Y. Ma, *Mater. Lett.*, 68 (2012) 336.
17. N. Venugopal, N. Arunakumari, M. G. Kim, K. Y. Sohn, *Int. J. Electrochem. Sci.*, 13 (2018) 5565.

© 2018 The Authors. Published by ESG ([www.electrochemsci.org](http://www.electrochemsci.org)). This article is an open access article distributed under the terms and conditions of the Creative Commons Attribution license (<http://creativecommons.org/licenses/by/4.0/>).